Welding in the World
https://doi.org/10.1007/s40194-024-01789-3

RESEARCH PAPER

Local relaxation of residual stress in high-strength steel welded joints treated by HFMI

Yuki Ono[1] · Heikki Remes[1] · Koji Kinoshita[2] · Halid Can Yıldırım[3] · Alain Nussbaumer[4]

Received: 26 September 2023 / Accepted: 10 May 2024

Abstract

This research studies the influence of high-peak loads on local relaxation of residual stress and fatigue damage in high-strength steel welded joints treated by high-frequency mechanical impact (HFMI) treatment. The joint behavior is simulated with elastic–plastic finite element analyses that account for the combined effect of geometry, residual stress, and material properties. This simulation uses two treated geometry models: with or without surface roughness on HFMI groove, and two material properties: S690QL and AH36 structural steels. The results show that surface roughness and load history, including high-peak loads, significantly influence fatigue response. It is revealed that the model neglecting the surface roughness cannot represent the amount of residual stress change and fatigue damage at less than 100 μm depth from the surface. In addition, the local yield strength in the HFMI-treated zone affects the plasticity behavior near the surface imperfection under the high-peak loads, which provides comparatively different fatigue damage between S690QL and AH36 in some cases. As a result, this study provides the further understanding needed to develop a robust modeling approach to the fatigue life estimation of HFMI-treated welds subjected to high-peak loads.

Keywords Residual stress · Relaxation · HFMI · High-strength steel · Welded joints · Surface profile · Surface roughness

1 Introduction

Lightweight, high-strength steel structures are demanded in various industrial applications such as offshore structures, ships, and bridges. The engineering challenge for this demand is improving the fatigue strength of welded joints since it is equal regardless of steel grades in current rules and standards [1, 2]. An effective tool to improve fatigue strength is the high-frequency mechanical impact (HFMI) treatment [3–12]. Applying HFMI treatment introduces compressive residual stress in the weld toe and material hardening in the surface layer, improving the local weld geometry, and removing typical weld defects. As a result, the crack initiation and growth periods within short crack lengths (typically with a depth of 0.2 mm) are predominant in the total fatigue life, resulting in significant fatigue strength improvement, especially for high-strength steel structures; see, e.g., [7, 13]. Marquis and Barsoum [14] proposed the fatigue design curves for HFMI-treated welds to consider this beneficial effect. However, these design curves are mainly based on experimental data and statistical analyses of fatigue test results. Thus, a deep understanding of failure mechanisms and phenomenological-based fatigue life estimation methods

Recommended for publication by Commission XIII—Fatigue of Welded Components and Structures.

✉ Yuki Ono
yuki.ono@aalto.fi

Heikki Remes
heikki.remes@aalto.fi

Koji Kinoshita
kinoshita@fukuoka-u.ac.jp

Halid Can Yıldırım
halid.yildirim@cae.au.dk

Alain Nussbaumer
alain.nussbaumer@epfl.ch

[1] Department of Mechanical Engineering, Aalto University, Espoo, Finland

[2] Department of Civil Engineering, Fukuoka University, Fukuoka, Japan

[3] Department of Civil and Architectural Engineering, Aarhus University, Aarhus, Denmark

[4] ENAC-RESSLab, Ecole Polytechnique Fédérale de Lausanne (EPFL), Lausanne, Switzerland

Published online: 03 June 2024

is still needed to develop a robust design criterion to ensure a high fatigue strength in engineering applications.

Welded steel structures in real situations can often experience a high-peak load, either a single overload or a part of variable amplitude loading. This type of loading may result in local material yielding and then the reduction in the compressive residual stress layer, i.e., relaxation of residual stress, which may suppress the effect of HFMI treatment [15–18]. To better understand the influence of residual stress relaxation on fatigue performance, studies by, e.g., Yonezawa et al. [16] and Loschner et al. [17] conducted extensive experimental measurements of residual stress change and stability under different cyclic loadings. In addition, numerical studies considering the dynamic elastic–plastic analysis of the HFMI process have been carried out by, e.g., Schubnell et al. [18] and Ruiz et al. [19]. The simulations were utilized for the analysis of residual stress relaxation. Mikkola et al. [20], Nazzal et al. [21], and Ono et al. [22] assessed fatigue damage related to crack initiation under various loading scenarios by using local strain and mean stress after the residual stress relaxation. The results have shown that residual stress relaxation greatly influences fatigue damage. For instance, in the study [22], the crack initiation most prone position along the surface of the HFMI groove was shown to shift due to a combination of stress concentration and residual stress relaxation effect. However, an idealized smooth HFMI geometry has been considered in numerical models used for these assessments. Thus, the influence of local plasticity at surface imperfections in the HFMI-treated regions on the residual stress relaxation and fatigue damage needs to be clarified for robust modeling of the crack initiation and short crack growth.

Concerning the plasticity behavior in the HFMI-treated regions, it is also crucial to clarify the impact of local elastic–plastic material properties on residual stress relaxation and fatigue damage. Schubnell et al. [23] showed that the steel grades affected the levels of residual stress relaxation. In the study [23], the change in residual stress by the compressive peak-loading was higher for the S960 steel grade than for the S355 steel grade in relation to the yield strength of the base material. It has been known that the degree of local hardness increases by work hardening from HFMI treatment is varied by different steel grades. For instance, experiments have indicated no increase in S960 steel grade [23] and slight increases like 1.1–1.4 times in S690 steel grades [24, 25], while great increases like 1.6–2.0 times in S355 steel grade [23, 24]. This can lead to different behavior of local plastic deformation at the surface imperfection. Thus, the local plasticity behavior due to different steel grades needs to be analyzed and compared to gain more insight into the mechanism of local relaxation of residual stress in high-strength steels.

Therefore, this study aims to clarify the local relaxation of residual stress in HFMI-treated welded joints made of two high-strength steels subjected to high-peak loading. The research shown in this paper is a continuation of works in [22, 26]. The study [26] experimentally investigated the fatigue behavior of HFMI-treated welded joint specimens using S690QL and AH36 at constant and variable amplitude loadings. Aiming to develop a robust modeling approach for fatigue life estimation of HFMI-treated welds, the following study [22] assessed the impact of residual stress relaxation on the actual crack initiation site of the HFMI groove surface for the S690QL specimens. This assessment was based on FE models considering a simplified smooth, treated geometry and local strain-based method. This paper differs from the previous investigation, taking into account an actual treated geometry in the FE models and focusing the investigations on the local fatigue response at potential crack initiation sites for the S690QL and AH36 specimens.

The workflow of the paper is the following. First, high-resolution geometry measurements were carried out to characterize HFMI geometry profiles as microstructurally accurate. Then, the local stress–strain response was studied with FE analyses to clarify the level of residual stress relaxation and mean stress after the residual stress relaxation. The FE model included the initial residual stress state, elastic–plastic material properties, HFMI-treated weld geometry, and load cycles, including high tensile and compressive peak loads. Based on the geometry measurements, this study defined the two types of HFMI geometry models: simplified HFMI geometry and actual HFMI geometry. The elastic–plastic material properties for S690QL and AH36 are considered in the FE simulation. Finally, the changes in residual stress due to the applied loads around surface imperfections, the influence of the model definition of HFMI geometry, and material mechanical property on residual stress relaxation and fatigue damage are discussed.

2 Experiment

2.1 Material and specimen details

This study used two types of structural steels, S690QL and AH36. The S690QL is the high-strength, quenched, and tempered steel. The AH36 is the high-strength shipbuilding steel. These steels have a thickness of 6 mm. The nominal yield strengths f_y for S690QL and AH36 are 832 MPa and 423 MPa, respectively. Figure 1 shows the configuration of the specimen. The constructional detail and data investigated in this paper consist of a plate with transverse non-load-carrying attachments and fillet welds in HFMI-treated states [26].

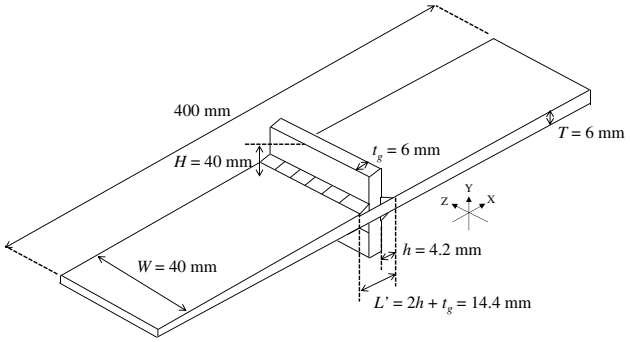

Fig. 1 Configuration of specimen [26]

2.2 Geometry measurements

Geometry measurements for the S690QL specimens were performed with a high-resolution line confocal imaging (LCI)-based measurement system. These measurements utilized Focalspec Oy's LCI 1600 sensor device [27]. The 2D cross-sections of the xy-plane in Fig. 1 were measured every 100 µm on each of the four welds of each specimen. The accuracy of measurements is about 1 µm, and datapoints were measured with 7 µm spacing in the *y* and *x* directions. A total of 532 cross-sections were used for the geometry analysis. Figure 2 shows an example of a 2D geometry profile. Microscopic surface roughness introduced by HFMI is captured in Fig. 2c. Weld size and HFMI-treated groove size were characterized by measuring the weld leg length (l_x, l_y), flank angle (θ), groove radius (ρ), groove depth (d), and groove width (w) from the 2D sections; see Fig. 2a and b. Table 1 shows the measurement results with average values and standard deviations.

3 Numerical analysis

3.1 FE models

FE simulations were performed on the specimens to clarify the relaxation of residual stress and fatigue damage. The global 2D model of the transverse attachment considered in this study is shown in Fig. 3. This study only focused on the behavior of HFMI-treated region, i.e., fatigue critical weld toe of non-load carrying fillet weld. Linear plane strain elements were used. Finite strain theory was applied to represent the large displacements and material non-linearity.

The FE models include partitions as shown in Fig. 3 to consider different material properties: base material (BM), weld metal (WM), heat-affected zone (HAZ), and HFMI-treated zone (HFMI). Combined non-linear isotropic-kinematic hardening parameters, so-called Voce-Chaboche's

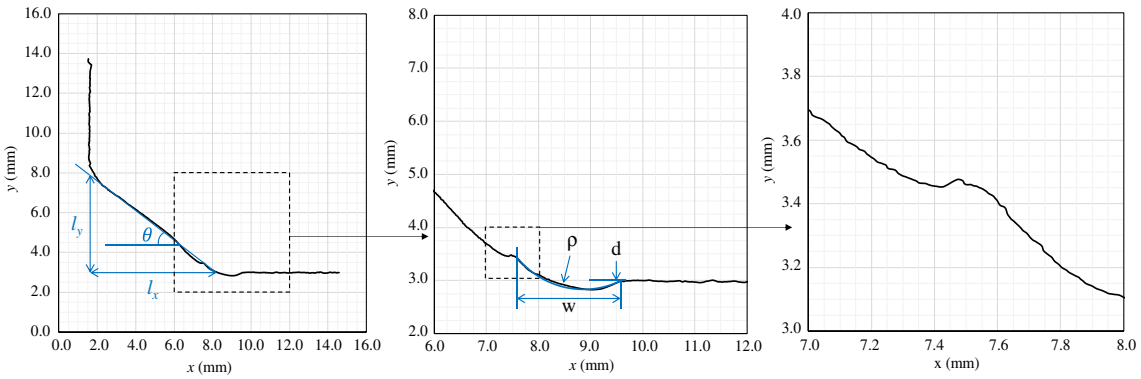

(a) Weld size (b) Groove size of HFMI-treated region (c) Surface roughness

Fig. 2 An example of 2D geometry profile around HFMI-treated region

Table 1 Measurement results of HFMI groove geometry and weld size

The number of sample	Flank angle, θ (°)		Weld length l_y (mm)		Weld length l_x (mm)		Groove radius, ρ (mm)		Groove width, w (mm)		Groove depth, d (mm)	
	Ave	Stdv	Ave	Stdv	Ave	Stdv	Ave	Stdv	Ave	Stdv	Ave	Stdv
532	35.1	2.55	4.67	0.43	6.64	0.35	1.87	0.24	2.42	0.30	0.13	0.04

Stdv standard deviation based on Gaussian log-normal distribution

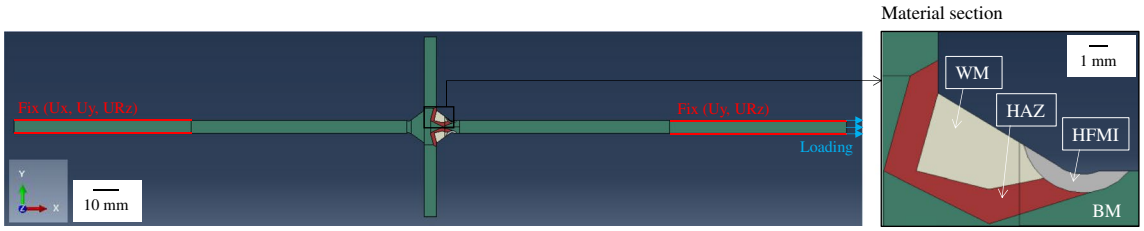

(a) Model shape and boundary condition (b) Material section

Fig. 3 Global model of transversal attachment

(VC) parameters, were employed. Table 2 provides the VC parameters for each material section of S690QL and AH36. These parameters were obtained by calibrating experimental cyclic hysteresis loops with a unique optimization algorithm called RESSPyLab [28]. Mikkola et al. [25] carried out fatigue tests using thin steel plates to clarify the cyclic response of S700MC BM, coarse-grain HAZ in MAG welded S700MC, and HFMI-treated S700MC. Since S700MC is similar steel grade to S690QL in this study, these fatigue test data were utilized to calibrate the VC parameters of BM, HAZ, and HFMI. The calibrations considered the first five hysteresis loops up to reaching stability. Young's modulus was pre-defined from the first tensile load of the test data [25] and not considered an optimization parameter, which better estimates crack initiation life for high-strength steel welded joints when little plasticity is involved [29]. As shown in Table 2, the cyclic test data for HAZ material show high hardening behavior after the first cycle, reflecting larger values of isotropic hardening parameters compared to others. For AH36, the VC parameters of E35 BM and HAZ in MAG-welded E35 as given in Petry et al. [30] were utilized. This study considered AH36 equivalent to E35 due to the same steel grade, and these VC parameters were similarly based on the predefined Young's modules from the initial tensile loads of test data [30]. Because the cyclic test data of HFMI for AH36 was not available in the current literature, the VC parameters were estimated from the BM property based on hardness distribution as similar to [31]. The cyclic yield strength of HFMI was defined by multiplying the hardness increase rate by the cyclic yield strength of BM. The hardness increase rate was 1.63 for HFMI, which was referred to in the previous hardness test results by Schubnell et al. [23]. In this case, an assumption was made that the isotropic and kinematic hardening parameters stayed the same as BM. With the same estimation and assumption, the VC parameters of WM for S690QL and AH36 were obtained based on the hardness test results by Yildirim et al. [26]. In the end, the increase rate of cyclic yield strength of HFMI compared to BM was about 1.15 for S690 and 1.63 for S355.

Figure 4 shows two types of HFMI geometry models. This study chose a representative HFMI geometry close to the average value among the measured profiles in Sect. 2.2. The simplified geometry model has the smooth geometries of the HFMI groove, which are 1.91 mm radius (ρ), 0.15 mm depth (d), and 2.8 mm width (w). In contrast, the actual geometry model directly incorporates the corresponding measured profile with surface roughness. The weld size of both models was the weld leg length of 4.75 mm for the base plate side (l_x),

Table 2 Voce-Chaboche's (VC) parameters for each material section

Material	Section	E [MPa]	σ_y [MPa]	Isotropic hardening		Kinematic hardening			
				Q [MPa]	q	C_1 [MPa]	γ_1	C_2 [MPa]	γ_2
S690QL	Heat-affected zone (HAZ)	208,000	530	140	104	16,448	285	13,233	285
	Base material (BM)	226,000	745	1	1	12,846	198	12,846	198
	Weld metal (WM)	226,000	781	1	1	12,846	198	12,846	198
	HFMI-treated zone (HFMI)	249,000	853	1	1	10,550	255	15,915	255
AH36	Heat-affected zone (HAZ)	209,000	404	1	1	13,511	167	11,026	167
	Base material (BM)	205,000	344	1	1	10,502	125	12,348	125
	Weld metal (WM)	205,000	468	1	1	10,502	125	12,348	125
	HFMI-treated zone (HFMI)	205,000	560	1	1	10,502	125	12,348	125

E Young modulus, Q maximum increase in size of yield surface due to hardening at saturation, q how quickly the increase of yield surface approaches the saturation, σ_y yield stress at zero plastic strain, C initial kinematic hardening modulus, γ rate at which the kinematic hardening modulus decreases with increasing plastic deformation

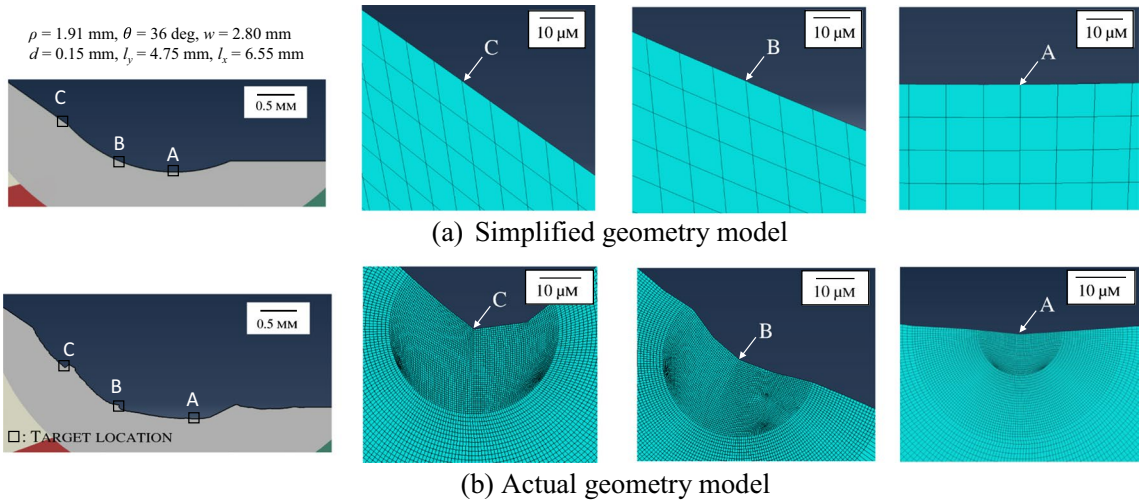

Fig. 4 HFMI geometry models and surface imperfections at Locations A, B, and C

6.55 mm for the gusset plate side (l_y), and the flank angle (θ) of 36°. These weld geometries were applied to both S690QL and AH36 models to compare the residual stress relaxation behavior at the same levels of stress and strain localization. This study investigated the stress–strain response at/near three target locations at weld toe, A, B, and C. A is the reference location corresponding to the HFMI groove bottom. B and C are the locations that can be possible crack initiation sites, according to the study by Ono et al. [22], and preliminary elastic stress analysis shows higher stress concentrations compared to other surfaces. To model local stress–strain behavior sufficiently in local surface imperfections, the element size around three locations was set to about 0.5 μm for the actual geometry models and then the size gradually increased towards the other global parts. In the case of the simplified model with smoother geometry, the element size was about 10 μm based on the results of the convergence study. The results showed that the mesh size of less than 10 μm provided almost the same stress gradient and less than 5.0% differences in the peak stress value. The required minimum element size is relatively larger as local surface imperfections do not exist.

Initial residual stress distributions implemented in the FE model are shown in Fig. 5. These residual stress distributions were based on the experimental measurement for HFMI-treated welded joints and represented by means of a predefined temperature field in Abaqus; see Ono et al. [22]. The changes in temperature through the plate thickness were applied at the nodes for three paths at $x = -3.5$ mm, 0 mm, and 3.5 mm, which created the self-equilibrated stress field in the treated area. The amounts of temperature changes for these three paths were calibrated by trial and error to find the best fit with the measured residual stress in the x-direction corresponding to the longitudinal direction of the specimen. The calibrated residual stress is the average value of scatter in measurement results from the study [22]. In addition, the residual stress field was compared with the experimental measurement data in the y and z directions. The comparison shows an agreement with the lower bound of scatter in measurement results. In-depth residual stress distributions at $x = 0$ had high surface compressive residual stresses of about $-0.60\,f_y$ within 0.5 mm depth, and then residual stress was gradually changed from compressive to tensile stress to be in equilibrium through plate thickness. Very near the surface, there is some variation (max 17%) in residual stresses between simplified and actual geometry models because of the roughness and imperfection effects. The distribution corrected by the yield strength f_y of the base material is used for both steels to have a solid comparison of the results. The f_y values for the correction are 832 MPa for S690 and 423 MPa for AH36. According to the previous study by Ono et al. [22], the residual stress close to the surface was similar for different steel grades if it is normalized by f_y.

The applied load cycles are depicted in Fig. 6. Three loading cases were compared to understand the impact of loading conditions on the residual stress relaxation and fatigue damage. Loading Case 1 is 20 cycles of constant amplitude loading (CAL) with $S_{max} = 0.47\,f_y$ and $S_{min} = 0.11\,f_y$. Loading Cases 2 and 3 include a high-peak load cycle with $S_{max} = 1.0\,f_y$ and $S_{min} = -0.43\,f_y$ and Loading Case 1. Loading Case 3 has the reversed order of tensile and compressive peak load compared to Loading Case 2. These loading histories were referred to as the highest and equivalent stress ranges used in variable amplitude loading in the study by Yildirim et al. [26]. The first single load assumed an extraordinarily large loading case in a part of service loading, such as in an earthquake, storm, or heavy sea wave. The following smaller 20 cycles are intended to represent the stress ranges due to cyclic fatigue loading that leads to high cycle fatigue and

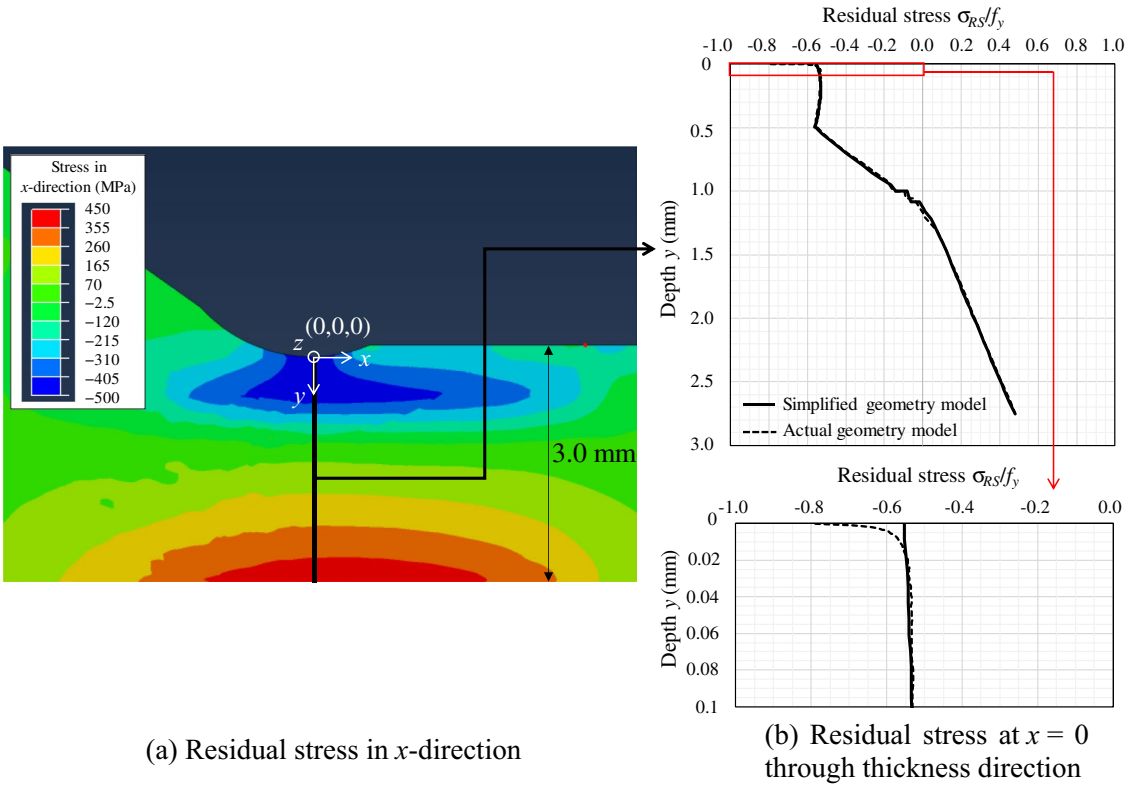

(a) Residual stress in x-direction

(b) Residual stress at $x = 0$ through thickness direction

Fig. 5 Implemented initial residual stress distribution in FE model (the left picture is S690QL simplified geometry model)

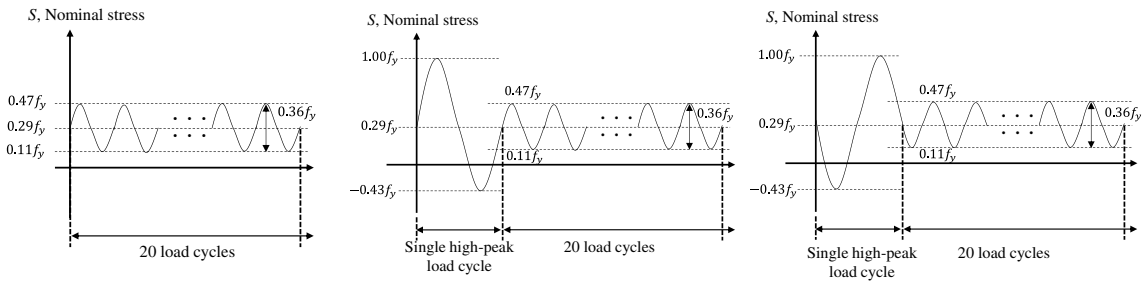

(a) Loading Case 1

(b) Loading Case 2

(c) Loading Case 3

Fig. 6 Applied load cycles for residual stress relaxation assessment

stabilized mean stress behavior. The same magnitude loading scaled with f_y was applied for both steels.

3.2 Fatigue-effective stress

After the FE simulation, this study assessed the effect of residual stress relaxation on fatigue damage required to initiate a microcrack. The fatigue damage can be represented by the Smith–Watson–Topper (SWT) parameter, as given in (1). The SWT allows for handling the mean stress/residual stress influence.

$$P_{\mathrm{SWT}} = \sigma_{\mathrm{eff,max}} \frac{\Delta\varepsilon_{\mathrm{eff}}}{2} \tag{1}$$

where $\sigma_{\mathrm{eff,max}}$ is the fatigue-effective maximum stress and $\Delta\varepsilon_{\mathrm{eff}}$ is the fatigue-effective strain range. Figure 7 shows the definition of fatigue-effective stress in this study. The fatigue-effective stress can be defined as an average value

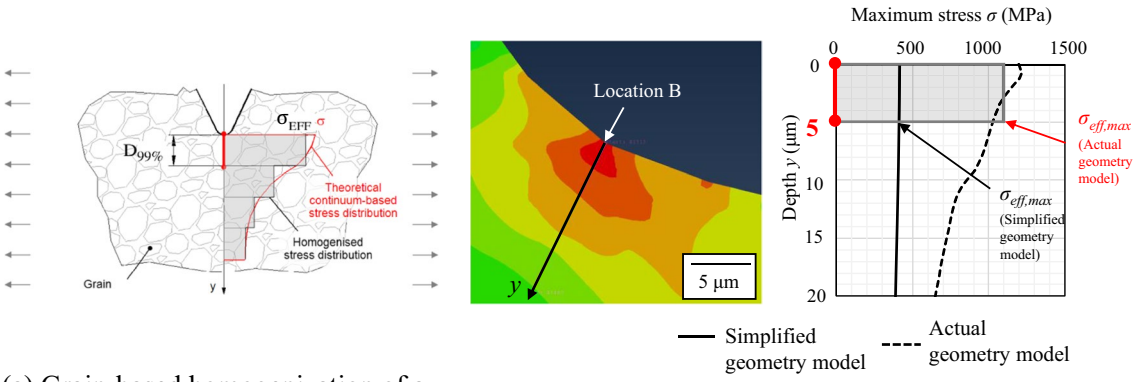

(a) Grain-based homogenization of a theoretical stress distribution [31]

(b) Example of averaging maximum stress

Fig. 7 Definition of fatigue-effective stress

over the representative volume element (RVE). The continuum-based modeling for RVE allows us to describe fatigue damage causing microscopic crack initiation and growth; see Remes et al. [32]. The equation for fatigue-effective stress is given in (2).

$$\sigma_{\text{eff}} = \frac{1}{d_{99\%}} \bullet \int_0^{d_{99\%}} \sigma dy \tag{2}$$

where $d_{99\%}$ is the grain size at a probability level of 99% as a material characteristic length, and σ is the maximum principal stress. In the actual geometry model, maximum principal stress distribution was averaged over $d_{99\%} = 5$ µm in the direction of axis y that starts from the tip of surface imperfection and is perpendicular to the direction of maximum principal stress. The fine grain size of $d_{99\%} = 5$ µm was determined with reference to grain size measurement results based on S700MC from Mikkola et al. [25] and S690QL from Garcia [33] and applied to all target locations. In the simplified geometry model, the maximum stress at 5 µm depth is considered fatigue-effective stress, corresponding to the stress at an integral point located in the center of 10-µm mesh. For simplicity, in this study, the results are compared distances from 5 to 100 µm, covering distances from short crack length to macro crack length.

4 Numerical results

4.1 Fatigue response in global regions

The change of residual stress can be divided into global and local behavior. In this section, the overall trend, i.e., global behavior of the residual stress change from HFMI-treated surface to mid-plane with respect to the applied load cycles, is presented. The local behavior near the surface imperfection in target locations is discussed in detail in Sect. 4.2.

Figure 8 shows the amount of residual stress change $\Delta\sigma_{\text{RS}}$ from the initial residual stress state to two geometry models, three loading cases, and two steel grades. The contour plots in Fig. 8 are expressed as

$$\Delta\sigma_{\text{RS}} = (\sigma_{\text{RS,AL}} - \sigma_{\text{RS,BL}})/f_{\text{y}} \tag{3}$$

where $\sigma_{\text{RS,BL}}$ is the initial residual stress before loading and $\sigma_{\text{RS,AL}}$ is the residual stress after loading. The difference in residual stress before and after loading is normalized by nominal yield strength f_{y} for the comparative comparison between S690QL and AH36. Positive value for $\Delta\sigma_{\text{RS}}$ is the decrease of compressive residual stress (i.e., relaxation) in the HFMI region, while the negative value is the increase of compressive residual stress in the HFMI region or the decrease of tensile residual stress above the deeper region than 1.2 mm from the HFMI groove bottom.

Loading Case 1 (CAL), typical for high-cycle fatigue ranges, did not show the residual stress change entirely; see Fig. 8a, d, g, and j.

For Loading Case 2 in Fig. 8b, e, h, and k, there were positive changes in residual stress inside of HFMI zones about 0.14 to 0.50 f_{y}, that is, the relaxation of compressive residual stress, especially beneath Locations A and B. However, the distribution of relaxation through the depth in the HFMI zone is different between S690QL and AH36. For instance, the simulation results in Fig. 8e and k showed, for S690QL, almost no change of residual stress near the surface and some degrees of relaxation at the subsurface of 0.2 to 0.5 mm depth, while for AH36, the significant relaxation from the surface to 0.8 mm depth. The area around Location C did not have a significant change of residual stress in any simulation results. About 1.2 to 3.0 mm depth from the surface indicated

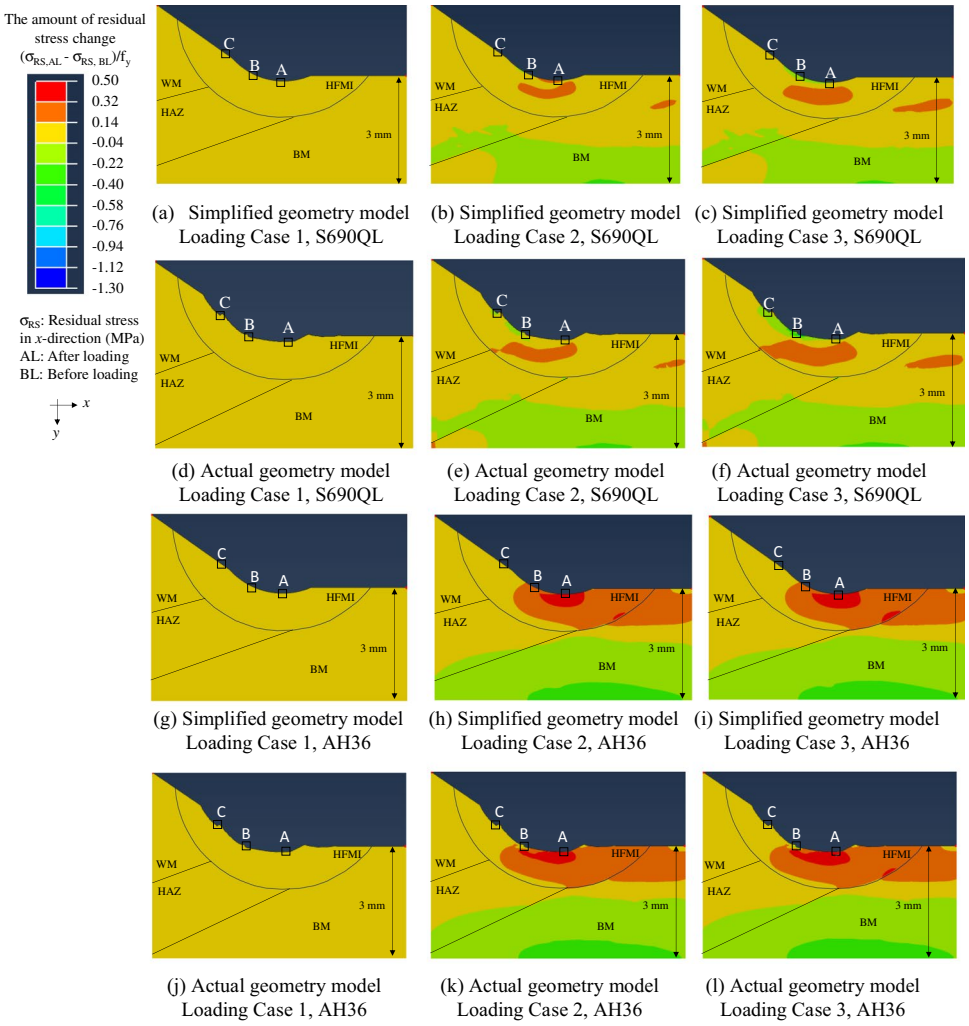

Fig. 8 The amount of residual stress change around HFMI-treated regions

negative changes in residual stress in HAZ and BM zones about -0.22 to $-0.40\ f_y$, that is, the reduction of tensile residual stress. According to the distribution of contours, the residual stress relaxation for AH36 tended to occur more significantly and widely than S690QL.

Loading Case 3 resulted in similar distributions of residual stress changes to Loading Case 2 in any simulation results. As one difference from Loading Case 2, the results for S690QL in Fig. 8c and f confirmed that the relatively wider near-surface regions in HFMI zones over Locations B and C have negative residual stress changes, i.e., inducing additional compressive residual stress.

In summary, the global trend in the change of residual stress is that the application of high-peak loading gives the residual stress towards zero, i.e., reducing compressive residual stress in the HFMI zone and tensile residual stress in the HAZ and BM zone. The effect of load sequence is the increase of compressive residual stress in the near-surface of the HFMI-treated region, which is apparent for S690QL mainly. The steel grades greatly affect the degree of residual stress relaxation and the area where the relaxation occurs. Both simplified and actual geometry models give similar results regarding the global behavior; thus, only the difference is due to load history and steel grades.

4.2 Fatigue response in local regions

To study the local fatigue response at the potential crack initiation sites, Fig. 9 presents the amount of residual stress change near the surface imperfection. Figure 10 shows the stress–strain responses extracted at the nodes with values close to fatigue-effective stress, which explains the mechanism of local change of residual stress. Only the data for Location B, the most critical among the three target locations, are shown in Figs. 9 and 10. Below, the main findings of these results are discussed.

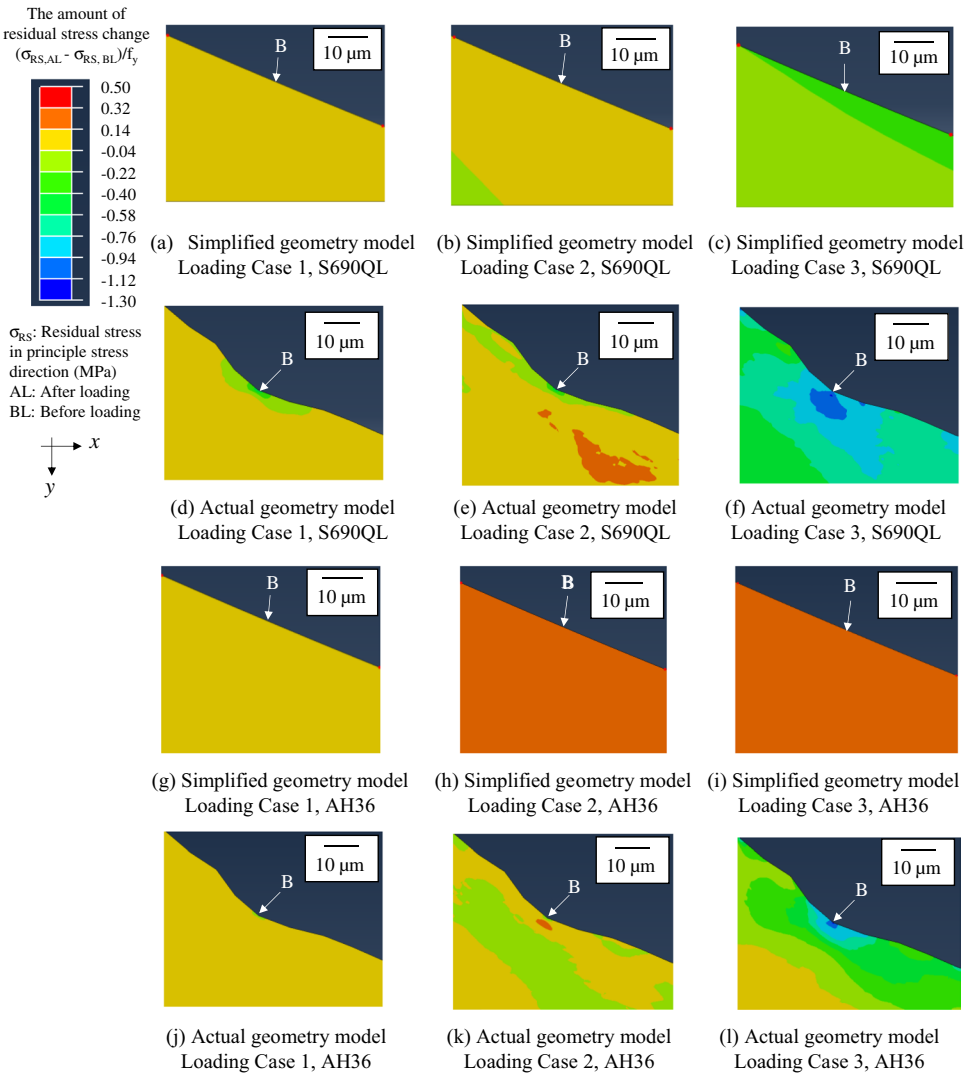

Fig. 9 The amount of residual stress change near surface imperfection for Location B

4.2.1 Effect of surface imperfection and load history on residual stress relaxation in S690QL

For the simplified geometry, the stress–strain responses remained the elastic behavior in Loading Case 1 (see Fig. 10a), and thus the change of residual stress did not occur as shown in Fig. 9a. The localized change occurred only for the actual geometry model in Fig. 9d. In this case, the surface imperfection at Location B generated high stress and strain localization. Thus, a 3.0 times increase in the resulting maximum stress and a 1.9 times increase in strain range compared to the simplified geometry model is observed. However, the change of residual stress is still so localized for the actual geometry model that the fatigue-effective stress–strain responses remained almost the elastic behavior; see Fig. 10d.

As Fig. 10b shows, the single peak load of Loading Case 2 resulted in the minor tensile yielding for the simplified geometry model. Thus, no significant change in residual stress before and after loading was found in Fig. 9b. In Fig. 10c, relatively larger tensile and compressive yielding took place for the actual geometry model. It is also worth noticing that after the peak-load cycle, the first CAL cycle involved the tensile yielding and contributed to the stability. As a result, the compressive residual stress stayed nearly the same as Loading Case 1 (see Fig. 9e), and so did fatigue-effective maximum stress.

For the simulation result in Fig. 10c, applying compressive peak load before the tensile one influenced the stress–strain response and then mean stress, like reducing maximum stress from 364 to 177 MPa in the simplified geometry model. Due to the tensile yielding only, the additional compressive residual stress was introduced, as observed in Fig. 9c. A more pronounced influence was seen on the actual geometry model; the tensile yielding was much more dominant in the elastic–plastic behavior, see Fig. 10f,

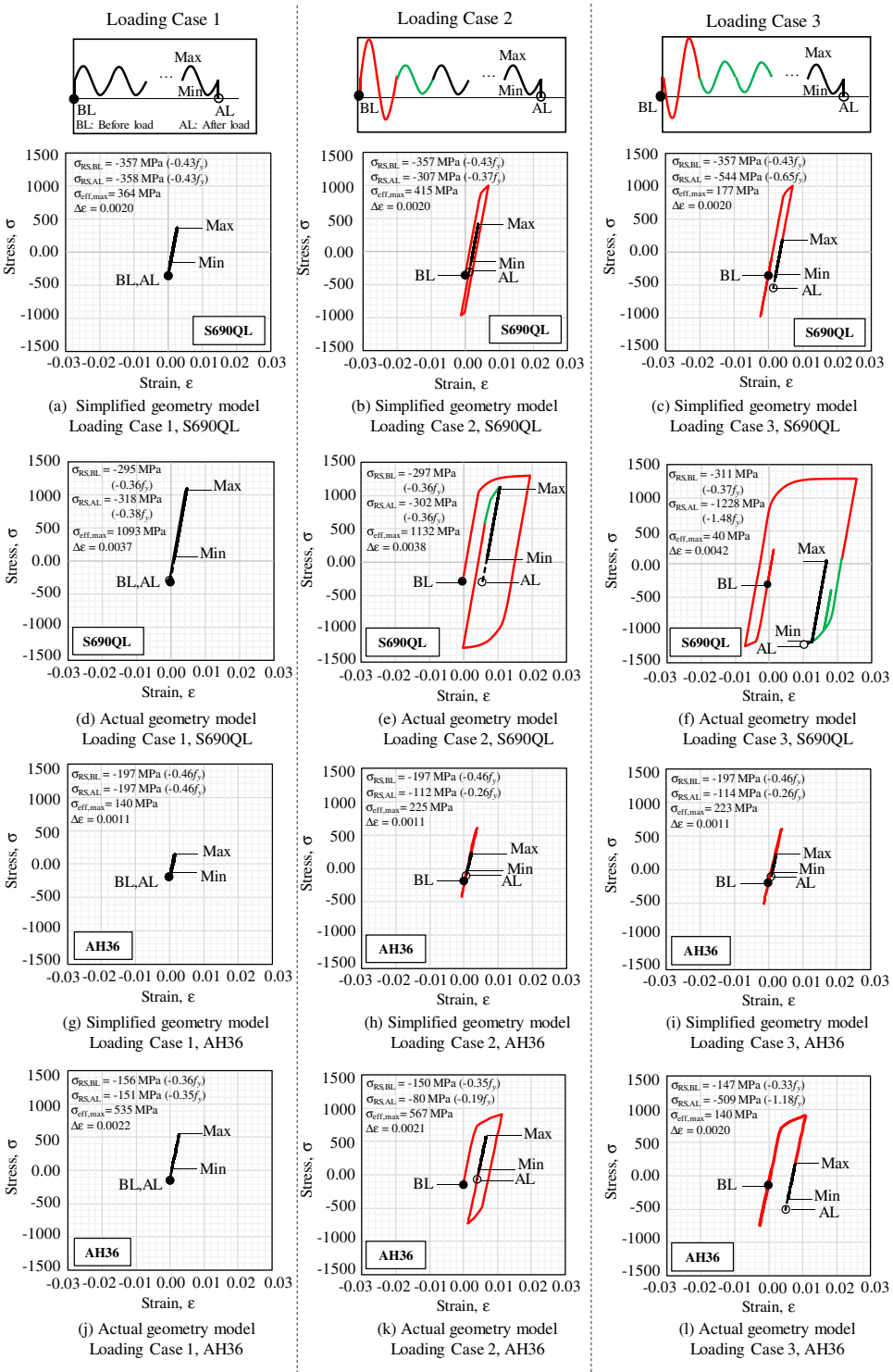

Fig. 10 Stress–strain responses at short crack initiation for Location B

and then inducing more significant compressive residual stress near the imperfection; see Fig. 9f. In addition, the fatigue-effective stress–strain response showed that after the peak-load cycle, two CAL cycles were taken until reaching stability for the actual geometry model. Consequently, most of the stress within the following CAL was below zero.

4.2.2 Effect of surface imperfection and load histories on residual stress relaxation in AH36

Similar to S690QL, the full elastic behavior was kept in AH36; see Fig. 10g and j. Thus, almost no residual stress relaxation was observed (see Fig. 9g and j). The comparison

between the simplified and actual geometry models for AH36 showed about 3.8 times increase in maximum stress and 2.0 times increase in strain range due to the surface imperfection, being higher than for S690QL in Sect. 4.1.1.

As Fig. 10h indicates, the first single peak load of Loading Case 2 involved little plasticity in the simplified geometry model. However, there was a relaxation of compressive residual stress after loading, according to Fig. 9h. This reduction can be due to the redistribution of residual stress from the alternation in other regions, as shown in Fig. 8h and k. On the other hand, the actual geometry model in Fig. 10k had the larger yielding behavior; both tensile and compressive yielding occurred in the peak-load cycle. After the peak load cycle, the stress–strain relationship immediately reached stability, which was different from the behavior in S690QL. Thus, the compressive residual stress was found to relax from − 150 to − 80 MPa. This relaxation corresponded to the very localized area near the surface imperfection in Fig. 9k. In the further depth, there was the increase of compressive residual stress, which was not seen in the S690QL simulation result.

In the case of Loading Case 3, the simplified geometry model had a similar stress–strain response to Loading Case 2; see Fig. 10i. Thus, there was the relaxation of compressive residual stress in Fig. 9i. According to Fig. 10l, the dominating tensile yielding in the first peak load increased the compressive residual stress from − 147 to − 509 MPa. This elastic–plastic behavior in AH36, except for the stability, was similar to S690QL. Figure 9l presents some increases of compressive residual stress near the imperfection, but its increase degree was lower than S690QL.

4.2.3 Effect of yield strength on maximum stress and strain amplitude

Figure 11 compares the maximum stress and strain amplitude for short crack initiation (at 5 µm distance) between S690QL and AH36 based on the actual geometry model. The results at a depth of 100 µm are also displayed to clarify if there is a similar effect in the deeper location assuming macro-crack length. They are extracted from the closed hysteresis loop of the last load cycle. For the comparative comparison, the maximum stress was normalized with f_y, and the strain range for AH36 was scaled up with the factor of 1.97 corresponding to f_y ratio of S690QL and AH36, that is, 832 MPa/423 MPa.

For the maximum stress in Fig. 11a, one can observe some results with almost identical values between S690QL and AH36. The main reason for this was no change or minor change of residual stress. Then, the stress localization effect from the surface imperfection mainly affected the maximum stress. On the contrary, the lower maximum stress in S690QL was found for Location C under Loading Case 2 and all locations under Loading Case 3. The difference was at most 6.60 times for Location B under Loading Case 3. For this reason, the residual stress after loading corrected by f_y was far different between S690QL and AH36. For example, for Location A under Loading Case 3, there was an increase of compressive residual stress of about 0.34 f_y for S690QL, but a decrease of compressive residual stress (i.e., relaxation) of about 0.24 f_y for AH36. This is attributed to different elastic–plastic behavior depending on the local cyclic yield strength. According to Fig. 11c, the lower maximum stress in S690QL was still found at 100 µm depth when Loading Case 2 and Case 3 were applied. This finding implies that the yield strength influences in-depth distributions of residual stress after peak loading and thus maximum stress.

Figure 11b indicates that there were much smaller variations in the strain ranges between S690QL and AH36 in comparison to the maximum stress. Any results were engaged to no plasticity at the last cycle of any loading cases. Thus, the yield strength did not significantly affect the strain ranges. The strain ranges for AH36 tended to be slightly higher than those for S690QL. The cause can be that the depth used for the calculation of strain ranges is slightly different, depending on the in-depth stress gradient after the loading, and Young's modulus of AH36 in this simulation is lower than that of S690QL. In Fig. 11d, there was a similar observation for the results at 100 µm depth with an even smaller difference between S690QL and AH36.

4.3 Fatigue damage analysis

The comparison of maximum stress for 5 µm distance (a representative for the start of short crack growth) and SWT parameter after the residual stress change between the S690QL simplified and actual geometry models for all locations was made, as shown in Fig. 12. This figure also indicates the data at a depth of 100 µm (a representative for the start of long crack growth) to show how the surface imperfection impacts the fatigue response below the surface. In Fig. 12a, the maximum stress at short crack initiation confirmed the large scatter due to the combination of the amount of residual stress change and stress localization effect from the surface imperfection. The degree of scatter highly varied with the loading condition and locations. At most, a 3.46 times difference in maximum stress between the two models was found on Location C under Loading Case 1. The results for 100 µm depth in Fig. 12b showed almost identical values between the two models due to less effect of surface imperfection and at most a 1.27 times difference for Location C under Loading Case 1. The results for the SWT parameter, as shown in Fig. 12c and d, gave certain increases of maximum errors when considering strain amplitudes. Other than that, there was almost the same trend in the variability of results as found by comparing the maximum stress.

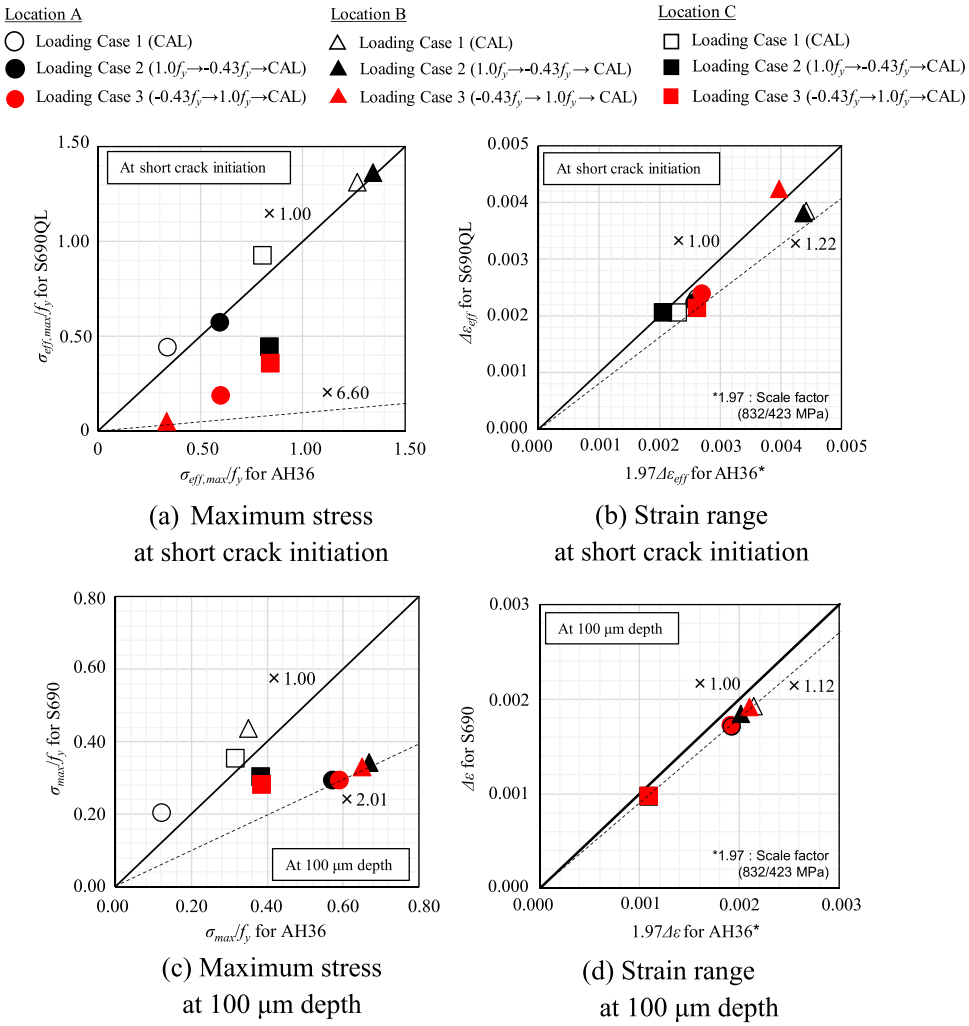

(a) Maximum stress at short crack initiation

(b) Strain range at short crack initiation

(c) Maximum stress at 100 μm depth

(d) Strain range at 100 μm depth

Fig. 11 Comparison of maximum stress and strain range between S690QL and AH36 actual geometry models for Locations A, B, and C

Similarly, the comparison results in the case of AH36 are illustrated in Fig. 13. At short crack initiation, the actual geometry model showed a large scatter in maximum stress and SWT parameter; see Fig. 13a and c. The level of scatter was nearly the same as S690QL according to the comparison of maximum differences. However, some results of AH36 were plotted differently from S690QL. These data corresponded to those with the comparatively large difference in the maximum stress after the residual stress change due to the effect of yield strength, as discussed in Sect. 4.2.3. The maximum stress and fatigue damage at 100 μm depth obtained a much smaller scatter between the actual and simplified geometry models, which was consistent with the trend in S690QL. It is worth noticing that for the actual geometry model, the result with the highest maximum stress and SWT parameter was Location B under Loading Case 1 in S690QL, while Location B under Loading Case 2 or Case 3 in AH36. This reflected the observation in Fig. 11c: the different maximum stress through the depth between S690QL and AH36.

5 Discussion

This study investigates the effect of surface roughness on residual stress relaxation and fatigue damage when the high-peak load is applied to HFMI-treated high-strength steel welded joints. The existing numerical approach for HFMI-treated joints is mainly based on simplified smooth geometries [20–22]; thus, the influence of surface roughness on residual stress relaxation and fatigue life estimation has been neglected. In this study, this influence is highlighted by comparing the simplified and actual HFMI geometry models. Furthermore, the results for two high-strength steels with different steel grades, S690QL and AH36, are compared to study the difference in the residual stress relaxation near the surface imperfection.

Section 4.1 shows how the overall trend in residual stress changes for HFMI-treated regions. When the high-peak load is included, the residual stress change happens in a large area from the near-surface of the HFMI zone to the middle plane of the BM zone. The load sequence effect is visible in the distributions of residual stress change in the

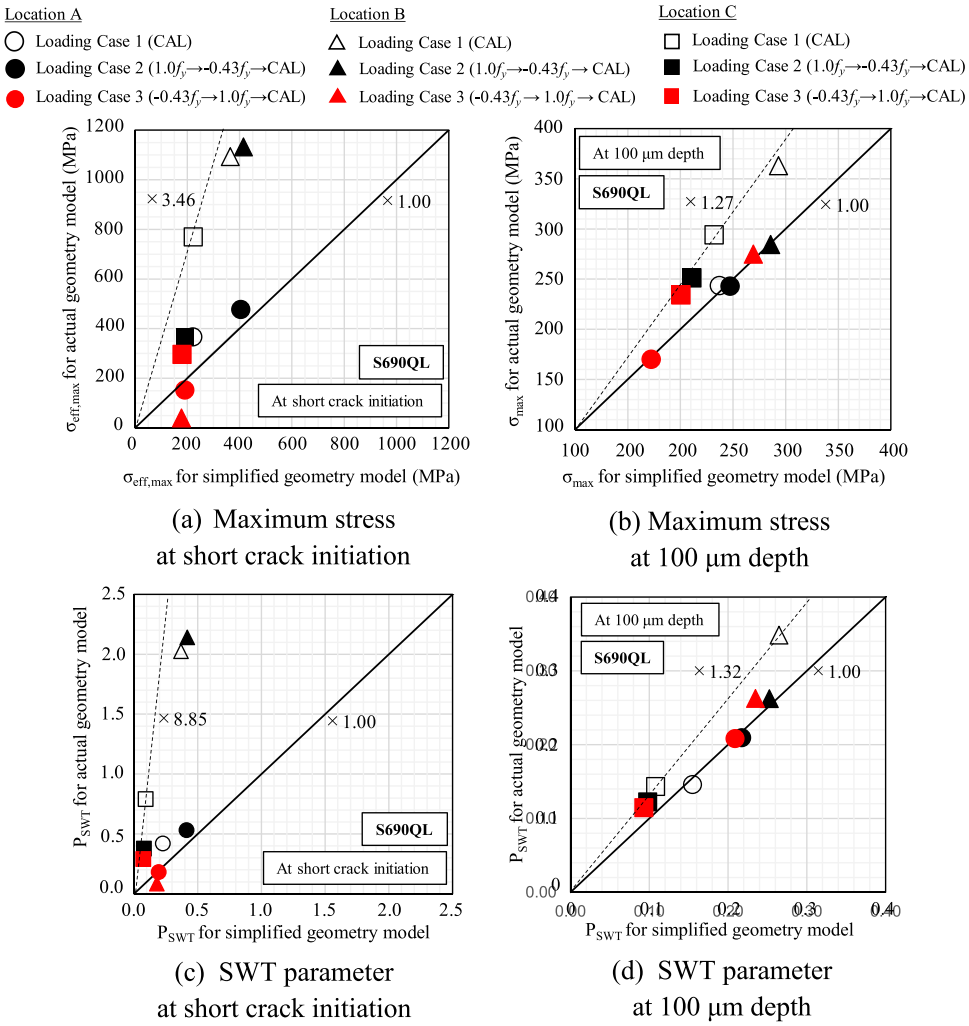

(a) Maximum stress at short crack initiation

(b) Maximum stress at 100 μm depth

(c) SWT parameter at short crack initiation

(d) SWT parameter at 100 μm depth

Fig. 12 Comparison of maximum stress and SWT parameter between S690QL simplified and actual geometry models for Locations A, B, and C

near-surface of HFMI zones. Steel grades noticeably influence the degrees of residual stress change and the change distributions through the plate thickness. AH36 tends to give more significant and wider changes of residual stress to HFMI-treated regions in comparison to S690QL. Both simplified and actual geometry models show almost the same tendency of global residual stress change as can be expected. Thus, little influence of surface roughness on the overall trend of residual stress change is revealed.

Section 4.2 studies the local change of residual stress near the surface imperfection. As opposed to the overall trend in Sect. 4.1, the local behavior of residual stress change depends not only on loading histories and steel grades but also on the definition of the geometry model. Applying the high-peak load brings a significant difference between the simplified and actual geometry models regarding the elastic–plastic behavior and the amount of plastic deformation; see Figs. 9 and 10. The load sequence effect is revealed more clearly in the actual geometry model. When the same magnitude of loading scaled by f_y is applied to the actual geometry model, there is a different behavior of residual stress change between S690QL and AH36. The steel grades are shown to differ in the local yielding behavior in the first peak load and the stability behavior in the following CAL cycles. In general, AH36 goes in minor plastic deformation and reaches stability when the peak load is over. This is related to the local cyclic yield strengths in HFMI zones that account for the hardening effect depending on steel grades: 115% increase rate for S690QL and 163% increase rate for AH36 in this study. AH36 has more decreases of compressive residual stress (i.e., more relaxation) in Loading Case 2 and fewer increases of compressive residual stress in Loading Case 3. Thus, the higher steel grades, like S690QL, relatively favor the local mean stress, i.e., less local fatigue damage, as shown in Fig. 11.

Section 4.3 clarifies the impact of local residual stress change on fatigue damage required to initiate a microcrack. From this section, the large variability in the resulting

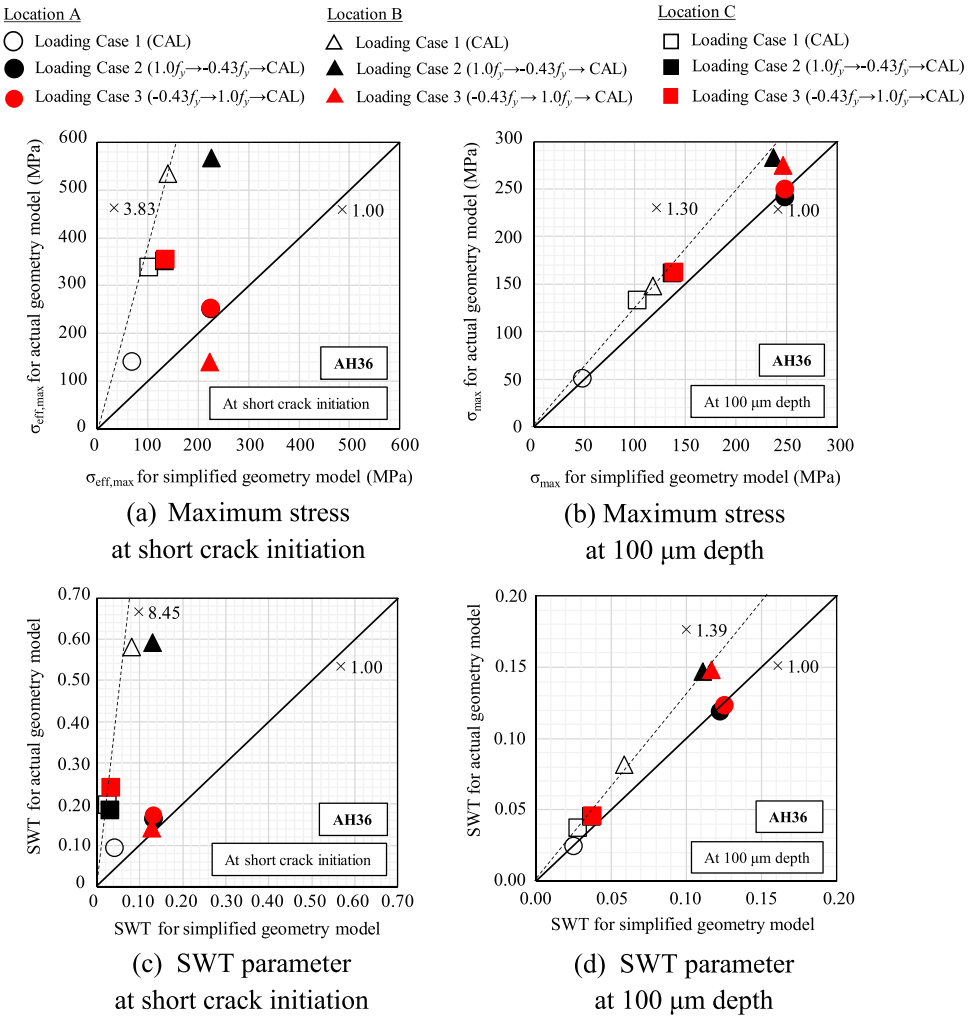

(a) Maximum stress at short crack initiation

(b) Maximum stress at 100 μm depth

(c) SWT parameter at short crack initiation

(d) SWT parameter at 100 μm depth

Fig. 13 Comparison of maximum stress and SWT parameter between AH36 simplified and actual geometry models for Locations A, B, and C

maximum stress and SWT parameter at short crack initiation (5 μm distance) can be observed in the actual geometry model for both S690QL and AH36. This variability level depends on the size and locations of surface imperfection, i.e., level of stress concentration, and material mechanical properties; see Figs. 12a and c and 13a and c. Compared with the SWT parameter curve as a function of the crack initiation life for the HFMI-treated S700 thin plate from Mikkola et al. [20], all the resulting SWT parameters by the S690QL simplified geometry model in this study are below the curve. This implies no fatigue crack initiation despite the fatigue failure happening for Loading Case 2 which corresponds to a tested condition (N_f = 258,750–492,000 cycles) in Yildirim et al. [26]. Thus, by missing the surface roughness, the model causes significant uncertainties in the local residual stress state, and fatigue response, accordingly, cannot estimate the crack initiation and short crack growth periods. Therefore, considering the effect of surface roughness contributes to developing the robust modeling approach for fatigue life estimation especially for HFMI-treated engineering components and structures that are exposed to high-peak loads. For the maximum stress and fatigue damage below the 100 μm depth or more from the surface, there is a relatively small difference between the actual and simplified geometry models, as Figs. 12b and d and 13b and d indicate. Thus, the simplified geometry model might be utilized for estimating long crack periods after the crack length of 0.1 mm or more, where linear fracture mechanics is assumed to be validated. To highlight the effectiveness of investigated numerical approach in this study, estimating fatigue life and comparison with the fatigue test results needs to be further studied in the future. Furthermore, future studies should clarify the physical role of influencing parameters in fatigue strength improvement and investigate robust quality limits of HFMI treatment.

6 Conclusion

This study performed the FE simulations to clarify the high-peak load effect on local relaxation of residual stress and fatigue damage in HFMI-treated high-strength steel welded joints. The elastic–plastic simulations simultaneously

accounted for the influence of surface roughness and residual stress to develop a robust modeling approach for crack initiation and short crack growth important for high-performing welds. In addition, the mechanism in the local evolution of residual stress in high-strength steels is studied by comparison with the results for two structural steels: S690QL and AH36. The following draws important findings in this study.

- If surface roughness exists in HFMI-treated welds, the simplified geometry model that neglects local geometry discontinues cannot represent the amount of residual stress change and fatigue damage at less than 100 µm depth from the surface.
- Considering actual HFMI-treated geometry with surface roughness in the elastic–plastic FE models is essential to a better understanding of failure mechanism and phenomenological-based crack initiation and short crack growth modeling.
- Besides surface roughness, the load history has a significant influence on fatigue response, but local relaxation of compressive residual stress does not always occur. For S690QL, with tensile ($1.0\,f_y$) and then compressive ($-0.43\,f_y$) high-peak load cycle leads to a minor change of the compressive residual stress near the surface imperfection on the HFMI groove, which does not greatly affect the increase of fatigue damage required to initiate a microcrack. Reversing the order of tensile and compressive high-peak load results in increasing the compressive residual stress and thus decreasing the fatigue damage.
- The comparison between S690QL and AH36 reveals different yielding behavior in the peak load cycle and stability behavior in the CAL cycles near the surface imperfection, related to the work hardening effect depending on steel grades. AH36 tends to have more decreases of compressive residual stress in the high-peak load and fewer increases of compressive residual stress in the reversed high-peak load. Thus, higher steel grades like S690QL work as favorably, i.e., less local fatigue damage when the same magnitude of loading scaled by f_y is applied.

Funding Open Access funding provided by Aalto University. This research was funded by the CaNeLis project from Business Finland with grant No. 3409/31/2022. The results of this research were presented in the Commission-XIII meeting in IIW 2023 with travel funding from Merenkulun säätiö. The financial supports are greatly appreciated.

Data availability The data in this paper are available from the corresponding author according to requests.

Declarations

Conflict of interest The authors declare no competing interests.

References

1. EN 1993 1–9. Eurocode 3 (2005) Design of steel structures: part 1–9: fatigue. European committee for standardization (CEN) Brussels Belgium
2. Japanese Society of Steel Construction (2012) Fatigue design recommendation for steel structures. Gihodoshuppan Co., Ltd (in Japanese)
3. Statnikov ES (1997) Application of operational ultrasonic impact treatment (UIT) technologies in production of welded joints. Annu Assem Int Inst Weld XIII-1667–97, Available online: http://www.appliedultrasonics.com/pdf/APPLICATIONS_OF_OPERATIONAL_ULTRASONIC_IMPACT_TREATMENT_(UIT)_TECHNOLOGIES_IN_PRODUCTION_OF_WELDED_JOINTS.html
4. Roy S, Fisher JW, Yen BT (2003) Fatigue resistance of welded details enhanced by ultrasonic impact treatment (UIT). Int J Fatigue 25:1239–1247
5. Huo L, Wang D, Zhang Y (2005) Investigation of the fatigue behaviour of the welded joints treated by TIG dressing and ultrasonic peening under variable-amplitude load. Int J Fatigue 27:95–101
6. Tominaga T, Matsuoka K, Sato Y, Suzuki T (2008) Fatigue improvement of weld repaired crane runway girder by ultrasonic impact treatment. Weld World 52:50–62
7. Weich I, Ummenhofer T, Nitschke-Pagel T, Dilger K, Eslami H (2009) Fatigue behaviour of welded high-strength steels after high frequency mechanical post-weld treatments. Weld World 53:322–332
8. Kudryavtsev Y, Kleiman J, Lobanov L, Knysh V, Prokopek G (2009) Fatigue life improvement of welded elements by ultrasonic peening. Annu Assem Int Inst Weld XIII-2010–04, Available online: https://itlinc.com/wp-content/uploads/2018/09/38_IIW_Doc_XIII-2010-04.pdf
9. Maddox SJ, Dore MJ, Smith SD (2011) A case study of the use of ultrasonic peening for upgrading a welded steel structure. Weld World 55:56–67
10. Yıldırım HC, Leitner M, Marquis GB, Stoschka M, Barsoum Z (2016) Application studies for fatigue strength improvement of welded structures by high-frequency mechanical impact (HFMI) treatment. Eng Struct 106:422–435
11. Yildirim HC (2017) Recent results on fatigue strength improvement of high-strength steel welded joints. Int J Fatigue 101:408–420
12. Leitner M, Barsoum Z (2020) Effect of increased yield strength, R-ratio, and plate thickness on the fatigue resistance of

high-frequency mechanical impact (HFMI)-treated steel joints. Weld World 64:1245–1259
13. Mori T, Shimanuki H, Tanaka M (2014) Influence of steel static strength on fatigue strength of web-gusset welded joints with UIT. J JSCE 70:896–900 **(in Japanese)**
14. Marquis G, Barsoum Z (2016) IIW recommendation on high frequency mechanical impact (HFMI) treatment for improving the fatigue strength of welded joints. Int Inst Weld. Springer, Singapore, pp 1–34
15. Tai M, Miki C (2012) Improvement effects of fatigue strength by burr grinding and hammer peening under variable amplitude loading. Weld World 56:109–117
16. Yonezawa T, Shimanuki H, Mori T (2020) Influence of cyclic loading on the relaxation behaviour of compressive residual stress induced by UIT. Weld World 64:171–178
17. Loschner D, Diekhoff P, Schiller R, Engelhardt I, Neitschke-Pagel T, Dilger K (2023) Residual stress stability of HFMI-treated transverse attachments under variable amplitude loading with the P(1/3) and the linear spectrum. Weld World 67:1545–1557
18. Schubnell J, Carl E, Farajian M, Gkatzogianis P, Knodel P, Ummenhofer T, Wimpory R, Eslami H (2020) Residual stress relaxation in HFMI-treated fillet welds after single overload peaks. Weld World 64:1107–1117
19. Ruiz H, Osawa N, Rashed S (2020) Study on the stability of compressive residual stress induced by high-frequency mechanical impact under cyclic loadings with spike loads. Weld World 64:1855–1865
20. Mikkola E, Remes H, Marquis G (2017) A finite element study on residual stress stability and fatigue damage in high-frequency mechanical impact (HFMI)-treated welded joint. Int J Fatigue 94:16–29
21. Nazzal SS, Mikkola E, Yıldırım HC (2020) Fatigue damage of welded high-strength steel details improved by post-weld treatment subjected to critical cyclic loading conditions. Eng Struct 237:111928
22. Ono Y, Yıldırım HC, Kinoshita K, Nussbaumer A (2022) Damage-based assessment of the fatigue crack initiation site in high-strength steel welded joints treated by HFMI. Metals 12(145):1–20
23. Schubnell J, Pontner P, Wimpory RC, Farajian M, Schulze V (2020) The influence of work hardening and residual stresses on the fatigue behavior of high frequency mechanical treated surface layers. Int J Fatigue 134:105450
24. Weich I (2011) Edge layer condition and fatigue strength of welds improved by mechanical post-weld treatment. Weld World 55:3–12
25. Mikkola E, Marquis G, Lehto P, Remes H, Hänninen H (2016) Material characterization of high-frequency mechanical impact (HFMI)-treated high-strength steel. Mater Des 89:205–214
26. Yıldırım HC, Remes H, Nussbaumer A (2020) A. Fatigue properties of as-welded and post-weld-treated high-strength steel joints: the influence of constant and variable amplitude loads. Int J Fatigue 138:105687
27. LMI Technologies (2023) Meet FocalSpec Line Confocal Sensors |LMI3D| LMI Technologies. https://lmi3d.com/family/smart-3d-line-confocal-sensors/
28. De Castro e Sousa A, Suzuki Y, Lignos DG (2020) Consistency in solving the inverse problem of the Voce-Chaboche constitutive model for plastic straining. J Eng Mech 146(9):04020097
29. Petry A, Gallo P, Remes H, Niemelä A (2022) Optimizing the Voce-Chaboche model parameters for fatigue life estimation of welded joints in high-strength marine structures. J Mar Sci Eng 10(818):1–20
30. Petry A (2022) Nonlinear material modelling for fatigue life prediction of welded joints in high strength marine structures, Master thesis, Aalto University, Aalto, Finland, Available online: https://aaltodoc.aalto.fi/items/99c84918-7fb0-462b-9419-2f478154331a
31. Remes H (2013) Strain-based approach to fatigue crack initiation and propagation in welded steel joints with arbitrary notch shape. Int J Fatigue 52:114–123
32. Remes H, Gallo P, Jelovica J, Romanoff J, Lehto P (2020) Fatigue strength modelling of high-performing welded joints. Int J Fatigue 135:105555
33. Garcia M (2020) Multiaxial fatigue analysis of high-strength steel welded joints using generalized local approaches. Ph.D Thesis, EPFL, Lausanne, Switzerland, Available online: https://infoscience.epfl.ch/record/279489?v=pdf